CrossMark

Accelerated degradation of yttria stabilized zirconia electrolyte during high-temperature water electrolysis

Aziz Nechache[1] · Bernard A. Boukamp[2] · Michel Cassir[1] · Armelle Ringuedé[1]

Abstract

The accelerated degradation of a commercial LSCF/YDC/YSZ/Ni-YSZ solid oxide electrolyzer cell ($La_{0.6}Sr_{0.4}Co_{0.2}Fe_{0.8}O_{3-\delta}$/ $Y_{0.1}CeO_{1.95}/Y_{0.08}Zr_{0.92}O_{1.96}$/Ni-YSZ) contaminated by Si-containing impurities is studied with time under up to -1.7 A cm^{-2} applied. Above ~ -0.6 A cm^{-2}, a new region appears in the polarization curve. This region corresponds to electronic conduction in the yttria-stabilized zirconia (YSZ) electrolyte, induced by the reduction under high current conditions. A shift in the typical frequencies (relaxation times) toward lower frequencies is then observed for the entire impedance spectra. This shift results finally in the disappearance of the positive loop related to the polarization resistance and the appearance of a negative (inductance type) loop which crosses the real axis (Z') at the lowest frequencies to become positive again. This is characteristic for an electrode process mode in which the electrochemical redox reactions vanish while the cell current becomes mainly electronic due to the reduction of the YSZ electrolyte. This trend increases with time. Such a characterization of the electronic conduction of the YSZ electrolyte by electrochemical impedance spectroscopy has not been reported to date under electrolysis mode, to the best of our knowledge. *Post-mortem* analysis by scanning electron microscopy coupled with energy dispersive X-ray spectroscopy (SEM/EDX) shows detrimental degradation of the electrolyte after only 360 h of overall testing duration with numerous micropores in the YSZ volume, and cracks and delamination at the yttria-doped ceria (YDC)/YSZ interface. EDX analysis reveals (i) a migration of La, Sr, Co, and Fe elements from lanthanum strontium cobalt ferrite (LSCF) anode to YDC layer and YSZ electrolyte and (ii) a very important shift of Ni from Ni-YSZ cathode to YSZ and YDC, and also to LSCF anode in a lower proportion. This study highlights the critical issue that impurities represent for solid oxide electrolysis cell operation.

Keywords Hydrogen · Solid oxide electrolysis cell · Electrochemical impedance spectroscopy · Degradation · Yttria stabilized zirconia · Electrolyte electronic conduction

Introduction

Hydrogen production through high-temperature electrolysis (HTE) is a clean and renewable alternative way to fossil fuel-based processes such as steam reforming, gasification of

✉ Aziz Nechache
   aziz.nechache@chimie-paristech.fr

✉ Armelle Ringuedé
   armelle.ringuede@chimieparistech.psl.eu

[1] Institut de Recherche de Chimie Paris, PSL Research University – Chimie-ParisTech – CNRS, 75005 Paris, France

[2] Department of Science and Technology & MESA Institute for Nanotechnology, University of Twente, P.O. Box 217, 7500 AE Enschede, The Netherlands

coal, and partial oxidation of heavy hydrocarbons [1–4]. In the case of water electrolysis, a solid oxide electrolysis cell (SOEC) is used to reduce H_2O to H_2 with electricity. Operating at high temperature, typically between 600 and 800 °C, allows reducing the amount of electrical energy needed balanced by thermal energy. Besides, no expensive catalyst such as Pt is needed. However, operating at high temperature favors cell degradation, one of the key issues that still prevent SOEC reaching economically viable performance/cost ratios in long-term work.

One possible source of severe cell degradation is electrolyte-related degradation. Stabilized zirconia, and especially yttria-stabilized zirconia (YSZ), is the most common material used as electrolyte in SOEC [3, 5]. However, YSZ still faces degradation issues, mainly after long-term operation or under high current densities, leading possibly to reduction of the material [3]. Several processes can lead to reduction of

stabilized zirconia, among which (i) controlling and monitoring oxygen partial pressure through oxygen pump or oxygen-trapping device, (ii) controlling the oxygen stoichiometry in oxide superconductors during solid-state electrochemical reactions, and (iii) wetting of zirconia by pure metals, alloys, or molten alloys [5–7]. Between the 1950s and the 1970s, various works focused on the conduction properties and mechanisms of stabilized zirconia with yttria, ceria, or calcia, and the rate-limiting mechanisms responsible for the onset of blackening [8–18]. These studies were followed by an investigation of Casselton on detrimental electrochemical reductions of polycrystalline and single crystals of stabilized zirconia consequently to the application of high current densities in the case of MHD (magnetohydrodynamics) electrodes [19]. Original electrochemical studies were carried out by Fabry and Kleitz to further understand the electrochemical coloration and redox reactions in solid ionic conductors, including stabilized zirconia [20]. In the 1990s, Janek et al. performed electrochemical reduction at 500 °C on both single crystals of YSZ and polycrystals of calcia-stabilized zirconia (CSY) [21]. More recently, the influence of the grain size on the redox stability of YSZ was evaluated by Boulfrad et al. [22]. Even if several reaction schemes have been suggested, discussion is still alive regarding the nature of the defects at the origin of zirconia blackening.

As mentioned above, cell degradation generally occurs from high applied current densities. Knibbe et al. examined the behavior of cells under high current densities (-1, -1.5, and -2 A cm^{-2}) for up to 900 h [23]. Important degradation of the cell was observed, characterized by a large increase in the electrolyte or series resistance, R_s, while increase in the polarization resistance, R_p, was not systematic. The observed R_s increase was attributed to oxygen formation in YSZ grain boundaries close to the Sr-doped LaMnO$_3$ (LSM)-YSZ/YSZ interface, based on the observation by transmission electron microscopy (TEM) and SEM of increased porosity and fractures in these YSZ grain boundaries. Such an increase of R_s was also noticed by Laguna-Bercero et al. in the case of a microtubular Ni-YSZ-supported cell with current densities up to -2.5 A cm^{-2} [24]. Also in this paper, it was attributed to YSZ electrolyte degradation with presence of voids and cracks at the grain boundaries, probably due to the electroreduction of the electrolyte. YSZ degradation under application of a high current was also reported by Kim et al. for a symmetrical cell LSM-YSZ/YSZ/LSM-YSZ operated for 120 h [25]. This was characterized by an increase of R_s attributed to intergranular fractures appearing along the YSZ electrolyte grain boundaries. An increase of the middle frequency part of the impedance diagram after starting the test was observed followed by the low-frequency part with time. These increases were associated with deactivation of LSM and densification of the O$_2$ electrode, respectively. Chen et al. tested several Ni-YSZ-supported cells at current densities above

-1 A cm^{-2} over a period of 1256 h [26]. In their case, degradation mainly occurred at the Ni-YSZ electrode with formation of ZrO$_2$ nano-particles on Ni surface, deteriorating Ni-percolation and possibly decreasing the density of triple phase boundaries (TPBs). It is suggested to be the result of Ni-YSZ interfacial reactions occurring under strong polarization conditions. Sun et al. studied the co-electrolysis of H$_2$O and CO$_2$ on several cells, applying -1 and -1.5 A cm^{-2} for up to 932 h [27]. Degradation of the cells was observed, and results from impedance measurements indicated that the initial degradation (first 100 h) was mainly due to an increase in R_p while the long-term degradation (above 100 h) was, as for Knibbe et al., caused to a large extend by an increase in R_s, indicating structural changes of the electrodes. Thus, based on the analysis of the difference in impedance spectra (ADIS) of the measured impedance diagrams, the gas shift study by electrochemical impedance spectroscopy (EIS), and conclusions from other studies made in solid oxide fuel cell (SOFC) mode [28–32], cell degradation at -1 A cm^{-2} was associated with the LSM-YSZ electrode, while both Ni-YSZ and LSM-YSZ electrodes were considered to contribute to cell degradation at -1.5 A cm^{-2}.

Schefold et al. tested a lanthanum strontium cobalt ferrite (LSCF)/YSZ/Ni-YSZ cell by applying -1 A cm^{-2} for 9000 h with a comparatively low degradation rate of 3.8% (40 mV)/1000 h [33]. In this case, impedance increase in the contribution from 10 kHz to 300 Hz was observed after 7615 h, here as well possibly associated with interfacial charge transfer [34–37]. Moreover, a similar impedance increase in the same contribution was also observed in initial measurements. Both observations support a possible H$_2$ electrode deactivation with time. Furthermore, increase in a small contribution with a phase peak at 30 Hz was observed, attributed by the authors to mass transport at the H$_2$ electrode. Nevertheless, impedance diagrams showed that important part of cell degradation was due to the ohmic contribution since large increase in R_s was observed with time. This study was completed by Tietz et al. with a post-test analysis of the cell by SEM and EDX [38]. Hence, cell degradation was mainly characterized by (i) internal pore formation in YSZ electrolyte due to cation migration; (ii) compositional inhomogeneities and cation demixing in the LSCF anode; and (iii) destabilization of the Ni-YSZ/YSZ interface due to material transport toward LSCF anode. This post-test analysis is in accordance with Schefold's impedance diagram analysis mentioned above [33]. More recently, Schefold et al. reported a 23,000-h (~2.6-year) electrolysis study performed on a scandia/ceria-doped zirconia electrolyte-supported cell [39]. A current density of -0.9 A cm^{-2} was applied for 20,000 h, with a voltage increase of only 0.57% (7.4 mV)/1000 h. The degradation observed was principally ohmic and mainly due to ionic conductivity decay in the electrolyte. Additional interesting studies are reviewed or reported elsewhere [3, 40–50].

Our previous work considered the appearance and evolution with time of a premature cell degradation resulting from the sealing of the cell holder and the support pieces providing and releasing H_2 electrode gas [4]. This degradation was characterized by a deformation of the i-U curve, several frequency shifts in the impedance diagrams, and the appearance of a new impedance contribution at the lowest frequencies assigned to a "reactivation" contribution. *Post-mortem* cell analysis by SEM/EDX revealed the presence of Si, Al, Na, K, and Ca at the H_2 electrode surface, a few ten microns deep from the surface and at the Ni-YSZ/YSZ interface. This degradation was associated with Si deposition, including at the Ni/YSZ/H_2O TPBs, and the reactivation contribution to an H_2O adsorption phenomenon. Si impurities originate from the glass sealant (Schott 8422) used to avoid H_2 electrode gas leakage between the cell holder and the support pieces. Analysis of the impedance diagrams allowed to clearly distinguish four to five contributions related to separate processes in the cell as identified by their respective time constants: (i) HF part ($f_0 = [100–1000$ Hz]; $C = 10$ mF cm^{-2}) associated with charge transfer at the Ni-YSZ/YSZ interface; (ii) MF1 part ($f_0 = 10$ Hz; $C = 100$ mF cm^{-2}) related to an H_2O diffusion phenomenon at the H_2 electrode; (iii) MF2 part ($f_0 = 1$ Hz; $C = 1$ F cm^{-2}) associated with H_2O gas conversion at the H_2 electrode; (iv) LF part ($f_0 = 0.1$ Hz; $C = 10$ F cm^{-2}) also related to an H_2O diffusion phenomenon at the H_2 electrode; (v) VLF part ($f_0 = [1–10$ mHz]; $C = |100$ F cm$^{-2}|$) associated with an H_2O adsorption phenomenon at the H_2 electrode. HF, MF, LF, and VLF correspond here to high frequency, middle frequency, low frequency, and very low frequency, respectively, while f_0 and C correspond to the relaxation frequency and the capacitance, respectively. A mechanism was proposed to explain the cell behavior after appearance of the premature degradation.

Using a similar methodology, we herein report that application of high current densities for a short duration to the cell contaminated by impurities containing Si leads to accelerated detrimental degradation consequently to electronic conduction of the YSZ electrolyte. This electronic conduction is clearly characterized by EIS, with appearance of an impedance contribution that, to the best of our knowledge, has not been reported to date under electrolysis mode.

Experimental

In this study, a LSCF//YSZ//Ni-YSZ commercial anode-supported SOFC used in HTE mode (HC Starck) was considered in a two-electrode experimental setup. An intermediate YDC (yttria-doped ceria) layer is present between LSCF ($La_{0.6}Sr_{0.4}Co_{0.2}Fe_{0.8}O_{3-\delta}$) and YSZ (yttria-stabilized zirconia, 8-YSZ). In the same way as our previous work [4], the cell holder and the support pieces providing and releasing H_2 electrode gas were sealed using Schott 8422 glass. A schematic of the experimental setup is shown in Fig. 1. More details of the cell and the experimental setup are given elsewhere [4, 34]. Figure 2 displays a SEM cross-section image of the different layers constituting the cell before the test. The cell was tested at 800 °C with $PH_2O/PH_2 = 5$ at the cathode side (50% H_2O +

Fig. 1 Schematic of the experimental setup used for this study. Based on [34]

permeable anode side

compression effort
(~2 kg/cm²)

N₂ or Air or O₂

I anode   *V* anode

gold wire

glass sealing
(Schott 8422)

current collectors

LSCF anode (Ø20mm)
YDC
YSZ electrolyte

Ni-YSZ cermet cathode (Ø50mm)

current collectors

cell holder +
H_2 electrode gas
inlet and outlet
(alumina)

Pt wire

I cathode   *V* cathode
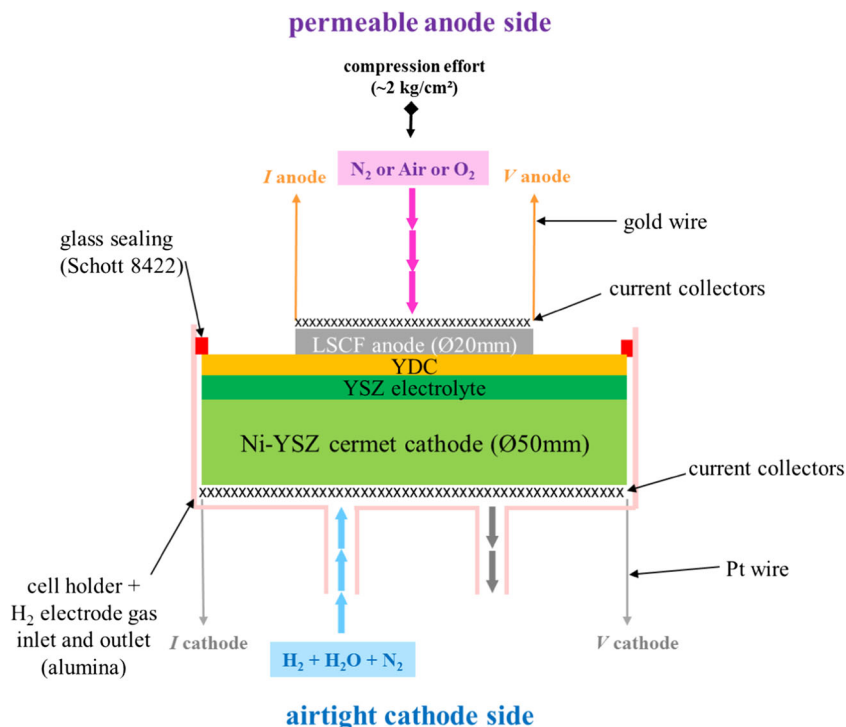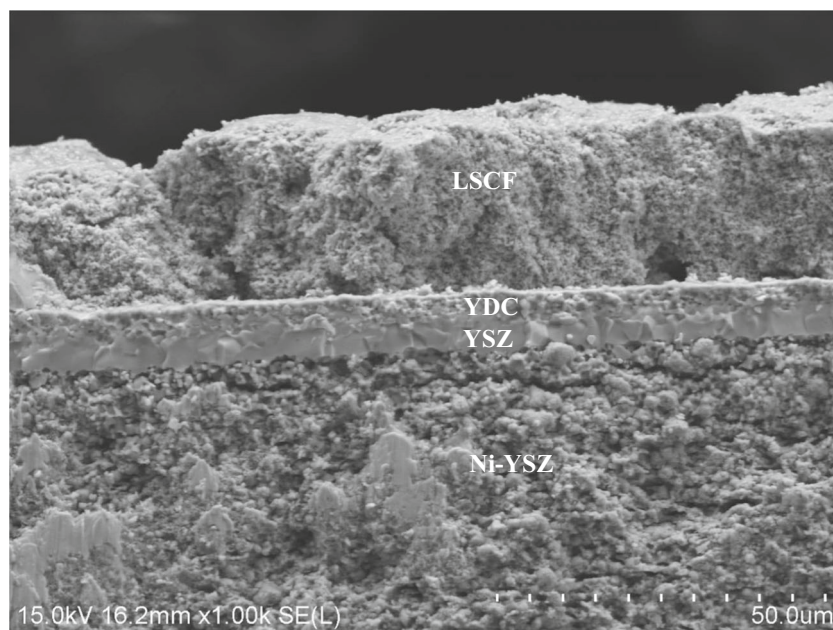
H₂ + H₂O + N₂

airtight cathode side

Fig. 2 SEM cross-section image of the different layers constituting the cell before the test, as follows from bottom to top: Ni-YSZ H_2 electrode, YSZ electrolyte, YDC intermediary layer, LSCF O_2 electrode

10% H_2 + 40% N_2), O_2 at the anode side, and a gas flow rate of 2.26 NL h^{-1} at each side. The results presented here were obtained between 288 and 360 h of test, *i.e.*, 72 h, with up to − 1.7 A cm^{-2} applied to the cell. A succession of impedance diagrams were measured, preceded and followed by current density-potential (*i-U*) curves. The overall 8-h procedure was performed nine times successively. Between 0 and 288 h of test, the same overall 8-h procedure was repeated with no more than − 0.6 A cm^{-2} applied to the cell, leading to the same behavior as what previously reported [4]. The *i-U* curves were recorded in potentiostatic mode with a rate of 1 mV s^{-1}. The electrochemical impedance diagrams were recorded applying a dc-current with a 30-mA amplitude perturbation in the frequency range from 10 kHz to 0.01 Hz with 10 points per decade. A Biologic SP-150 frequency analyzer with a 20-A booster was used for both chronopotentiometry and EIS measurements. *Post-mortem* analyses of the tested cell were performed using a Hitachi SU-70 SEM-FEG equipped with an Oxford X-Max 50 mm^2 X-ray microanalysis system for the energy-dispersive X-ray spectroscopy (detection limit: 1.0 wt%). In our case, analyses were carried out with an acceleration voltage of 1 and 5 kV. No additional coating was required to clearly observe by SEM the surfaces and the considered layers.

Results and discussion

Appearance of YSZ electronic conduction

In a similar study recently reported [34], the *i-U* curve measured showed three functioning regions: region I where R_p

(referring to the polarization resistance) decreases with increasing current densities corresponding to a decrease in the activation resistance; region II where R_p reaches a minimum and remains constant while current density increases showing an optimal use of the cell; and region III where R_p increases with current density resulting mainly from an increase of concentration overpotentials. As previously introduced [4], in the present study, these regions are affected by the deposition of Si-containing impurities, leading to the appearance of two additional functioning regions corresponding to the cell reactivation (region IV) until limitation by H_2O transport becomes the predominant phenomenon governing the cell functioning (region V). According to Fig. 3, above − 0.6 A cm^{-2} applied, the system does not remain in the region V defined before where H_2O transport limitation dominates the cell functioning [4]. A new region appears, region VI, characterized by a slope change of the *i-U* curve. According to Fig. 4a, this slope change corresponds to a significant decrease of the total resistance R_t which is equal to 3.4 Ω cm^2 for − 0.6 A cm^{-2} and reaches 123 mΩ cm^2 for − 1.5 A cm^{-2} (after 288 h). Figure 4b shows that the appearance of region VI is also characterized by a large increase of the ohmic resistance R_s. Indeed, R_s, equal to 270 mΩ cm^2 on average between 0 and − 0.6 A cm^{-2}, increases to stabilize at 380 mΩ cm^2 above − 1.0 A cm^{-2}, which means a 29% increase. Figure 4c shows that the polarization resistance R_p decreases in the same way as R_t from − 0.6 A cm^{-2}. However, contrary to R_t, this decrease is so large that R_p becomes negative above − 0.9 A cm^{-2}, reaching − 258 mΩ cm^2 for − 1.4 A cm^{-2}. All this suggests that the appearance of region VI results from an electronic conduction of the YSZ electrolyte. Indeed, the *i-U* curve slope occurs for a cell voltage of 1.57 V. According to
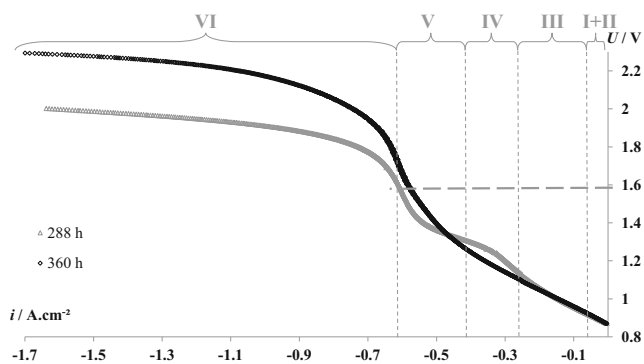
Fig. 3 Polarization curve (*i-U* curve) of the cell after 288 h (△) and 360 h (◊) of test. The *i-U* curve measured shows six functioning regions: region I corresponding to a decrease in the activation resistance, region II to an optimal use of the cell, region III resulting mainly from an increase of concentration overpotentials, region IV corresponding to the cell reactivation until limitation by H_2O transport becomes the predominant phenomenon governing the cell functioning (region V). Above −0.6 A cm^{-2} applied, region VI appears, resulting from an electronic conduction of the YSZ electrolyte characterized by a slope change of the *i-U* curve. $T = 800$ °C, $P_{H2O}/P_{H2} = 5$ with 50% H_2O + 10% H_2 + 40% N_2 (H_2 electrode), O_2 (O_2 electrode), standard flow rate of 2.26 NL h^{-1} on both sides

Boulfrad et al., it is known that, in the case of YSZ electrolyte and with the conditions of this study, YSZ electronic conduction phenomenon appears from 1.5 V after deduction of the ohmic voltage drop [22]. More generally, when the cell is under a significantly increased current demand while in the gas transport limitation regime, a reduction of the electrolyte, which becomes partially electronically conductive, occurs. The voltage then remains almost constant while the current increases quickly. In the case of YSZ electrolyte, this phenomenon appears between 1.5 and 1.9 V at $T = 800$ °C [51, 52]. Hence, R_t and R_p decrease, resulting from a change in the "functioning mode" of the cell. Indeed, from − 0.6 A cm^{-2}, current circulation is less based on the electrochemical redox reactions at the electrode/electrolyte interfaces, in favor of the less resistive YSZ electronic conduction. This change becomes more important when the current applied increases, the system favoring the less resistive "functioning mode", until − 0.9 A cm^{-2} above which R_p is zero and finally negative, which means that the current is henceforth mainly circulating via YSZ electronic conduction. On the other hand, an increase in R_s is characteristic of the YSZ electrolyte degradation resulting from a use of YSZ which goes against the intrinsic property of this material, *i.e.*, the very low electronic conductivity.

Figure 5 contains the impedance diagrams recorded for different current densities applied corresponding to region VI after 288 h of test. Figure 5a shows that the appearance of YSZ electronic conduction leads to a contraction of the whole impedance diagram characteristic of the R_t drop from 5.2 to 0.6 Ω cm^2 between − 0.6 and − 0.8 A cm^{-2}. Thus, all the main phenomena governing the cell functioning so far, *i.e.*, charge
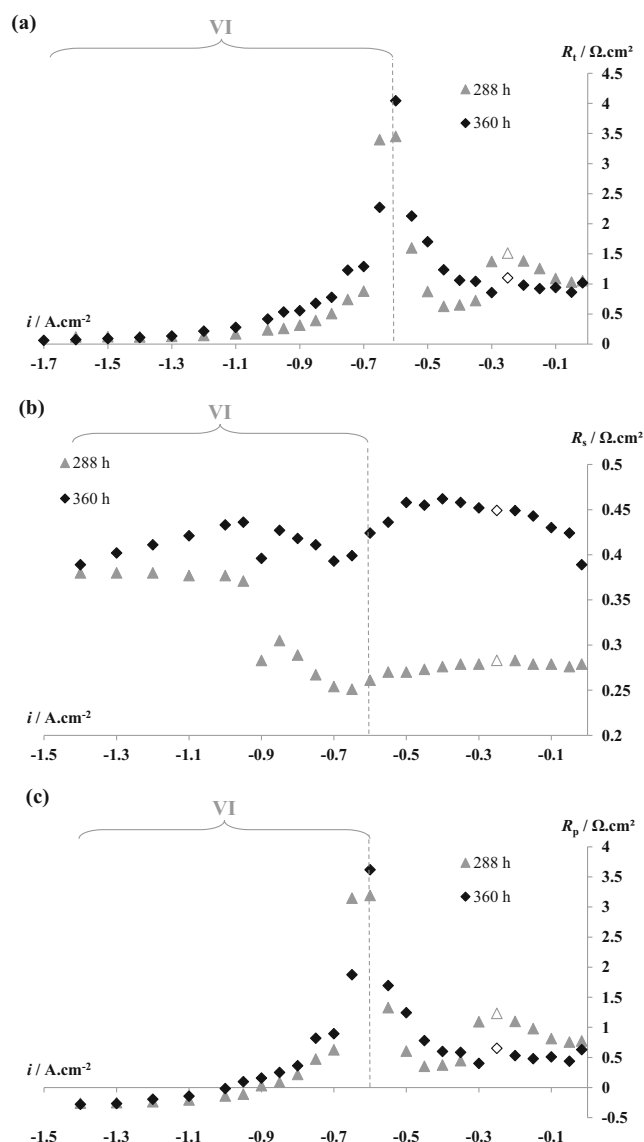

Fig. 4 **a** Total R_t, **b** ohmic R_s, and **c** polarization R_p resistances of the cell after 288 h (△) and 360 h (◊) of test. $T = 800$ °C, $P_{H2O}/P_{H2} = 5$ with 50% H_2O + 10% H_2 + 40% N_2 (H_2 electrode), O_2 (O_2 electrode), standard flow rate of 2.26 NL h^{-1} on both sides. The open symbols correspond to the appearance of the reactivation contribution [4]

transfer and H_2O transport phenomena at the Ni-YSZ electrode, are now less involved because of this electronic conduction. R_t decrease continues between − 0.8 and − 1.0 A cm^{-2}, as illustrated in Fig. 5b. Besides, the contraction of the impedance diagram is accompanied by a frequency shift of the whole diagram to the lowest frequencies, starting when *i* changes from − 0.6 to − 0.7 A cm^{-2}. This trend continues above − 0.7 A cm^{-2} with the appearance, at − 0.8 A cm^{-2}, of a kind of "knot" at the lowest frequencies which suggests the beginning of a new contribution. This trend is still present at − 0.9 A cm^{-2} before a radical change at − 1.0 A cm^{-2}. Indeed, as observed in Fig. 5c–d, from − 1.0 A cm^{-2}, the positive arc of the diagram corresponding to R_p decreases, to finally disappear at − 1.2 A cm^{-2},
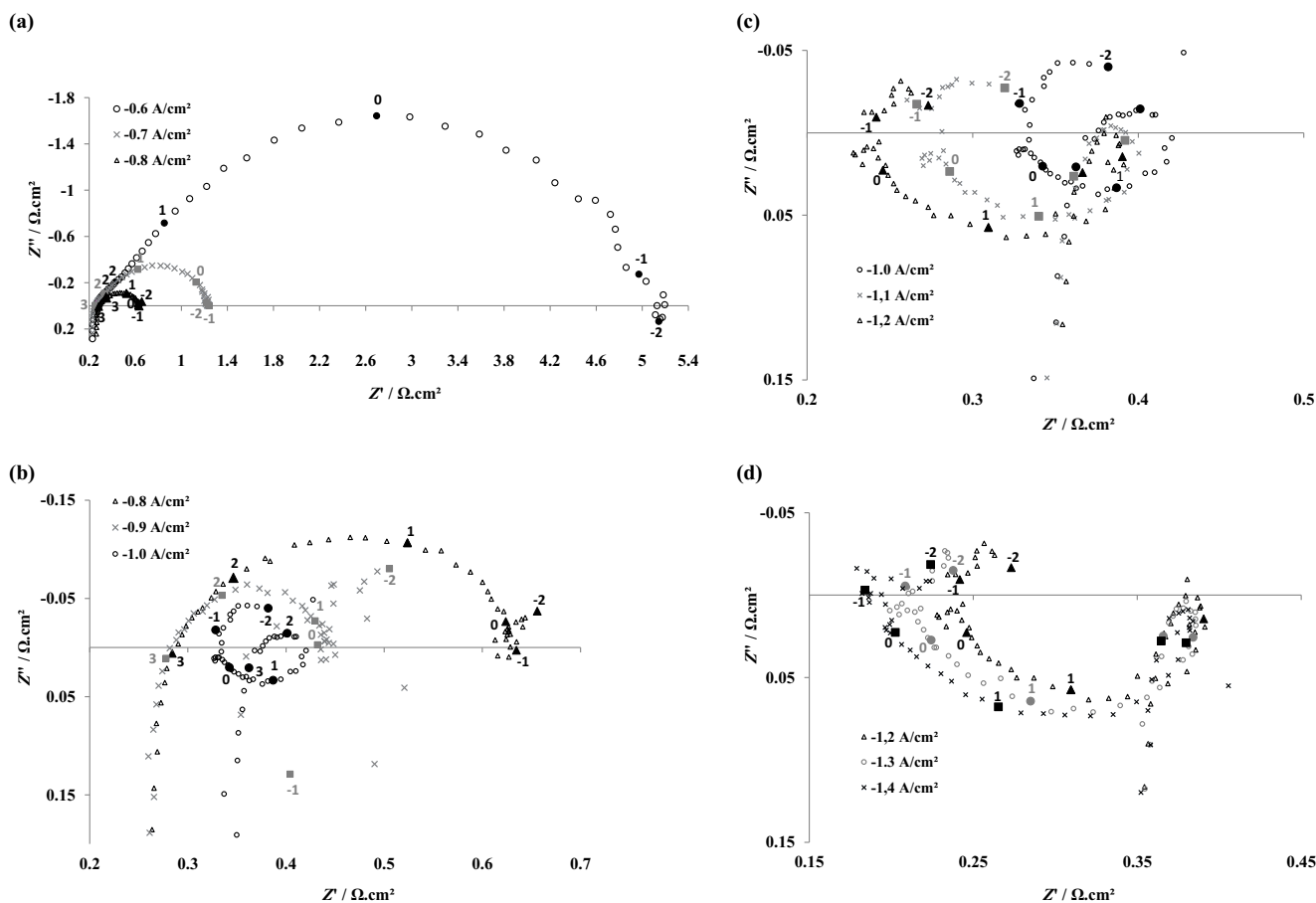
(a)

(b)

(c)

(d)

Fig. 5 a–d Impedance diagrams measured between − 0.6 and − 1.4 A cm⁻² after 288 h of test. $T = 800$ °C, $P_{H2O}/P_{H2} = 5$ with 50% $H_2O + 10\% H_2 + 40\% N_2$ (H_2 electrode), O_2 (O_2 electrode), standard flow rate of 2.26 NL h⁻¹ on both sides. It should be noted that from $i = − 0.9$ A cm⁻², R_p was calculated based on R_s and R_t values obtained from the impedance diagrams and the i-U curve, respectively

in favor of a negative loop which crosses the real axis (Z') at the lowest frequencies to become positive. This negative loop becomes more dominant with further increased current density. Consequently, the passing of R_p to negative values coincides with the radical trend change observed at − 1.0 A cm⁻², characteristic of a "functioning mode" where the phenomena associated with the electrochemical redox reactions are no longer involved. Moreover, the frequency shift of the impedance diagram toward the lowest frequencies until appearance of this combined "negative ➔ positive" loop is characteristic of the YSZ electronic conduction phenomenon.

Evolution with time of YSZ electronic conduction

In order to study the evolution of the YSZ electronic conduction phenomenon with time, the cell is considered after 72 additional hours, which means 360 h of total test duration. Figures 3 and 4a show a change in the cell behavior: the polarization curve at 360 h (Fig. 3) presents a quasi linear trend until − 0.3 A cm⁻² followed by a slope increase until − 0.6 A cm⁻². However, even if R_t variations between 0 and − 0.4 A cm⁻² are not very

important, regions I to IV are still distinguishable between 0 and − 0.3 A cm⁻² as well as region V between − 0.3 and − 0.6 A cm⁻² (Fig. 4a). Region VI is then reached from − 0.6 A cm⁻², but in this case for a voltage of 1.67 V, higher than 1.57 V at 288 h. It should be noticed that with time, R_t decreases between 0 and − 0.3 A cm⁻², increasing thereafter. In addition, R_t variations with time are relatively small. To better understand these observations, R_s and R_p are further considered.

Figure 4b shows a large increase of R_s with time, particularly between 0 and − 0.5 A cm⁻² (for $i = − 0.3$ A cm⁻², $R_s = 452$ mΩ cm² at 360 h against 283 mΩ cm² at 288 h). Nevertheless, above − 1.0 A cm⁻², R_s tends to the same value whatever the functioning time considered. Figure 4c shows that with time, in the same way as R_t, R_p decreases between 0 and − 0.3 A cm⁻² and increases then. Moreover, just as R_t, R_p variations are relatively small with time. This is the consequence of the evolution with time of the cell "functioning mode" with part of the current circulating by YSZ electronic conduction and not from the electrochemical redox reactions. The large increase of R_s with time, as observed before, is relevant for this interpretation.
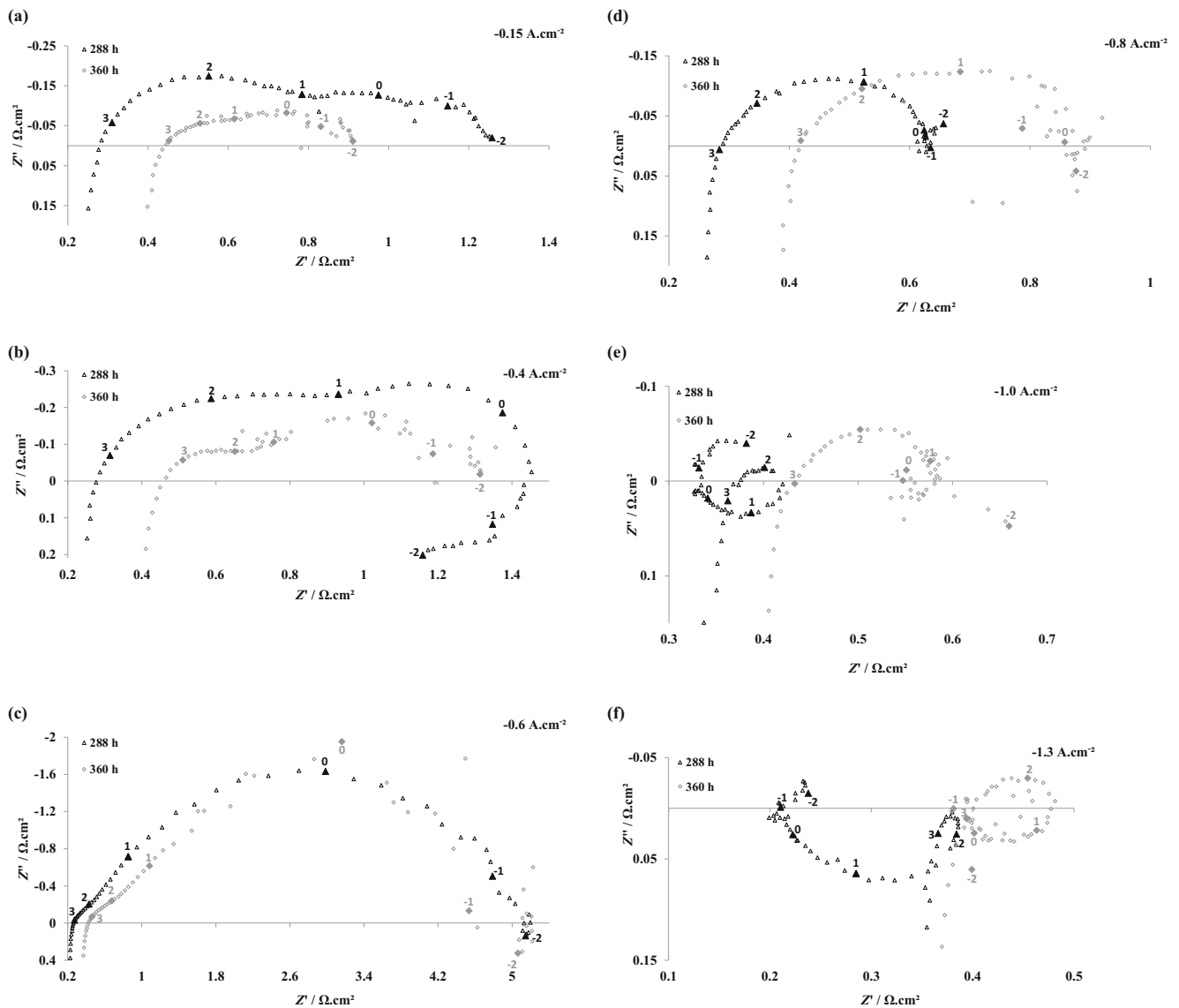
Fig. 6 Impedance diagrams measured at **a** − 0.15 A cm^{-2}, **b** − 0.4 A cm^{-2}, **c** − 0.6 A cm^{-2}, **d** − 0.8 A cm^{-2}, **e** − 1.0 A cm^{-2}, and **f** − 1.3 A cm^{-2} after 288 h (△) and 360 h (◇) of test. $T = 800$ °C, $P_{H2O}/P_{H2} = 5$ with 50% H_2O + 10% H_2 + 40% N_2 (H_2 electrode), O_2 (O_2 electrode), standard flow rate of 2.26 NL h^{-1} on both sides. It should be noted that from $i = -0.4$ A cm^{-2}, R_p was calculated based on R_s and R_t values obtained from the impedance diagrams and the i-U curve, respectively

Figure 6 contains the impedance diagrams recorded for different current densities at 288 h and 360 h. It can be seen from Fig. 6a that, observed with time, the decrease in R_p between 0 and − 0.3 A cm^{-2} is characterized by a contraction of the whole impedance diagram. Hence, the impedance of all the phenomena associated with redox reactions, and governing the cell functioning, decreases with time for the lowest current densities applied. This is a direct consequence of the partial circulation of the cell current by YSZ electronic conduction. Between − 0.3 and − 0.6 A cm^{-2}, contrary to the functioning at 288 h, there is no reactivation contribution anymore at 360 h (Fig. 6b). That is why R_p increases with time in this current density range. Nevertheless, the impedance of

all the phenomena associated with the redox reactions continues to decrease with time in this current density range, meaning that part of the current is still circulating by YSZ electronic conduction. From − 0.6 A cm^{-2} (Fig. 6c), the same frequency shift of the whole diagram to the lowest frequencies is observed between 288 and 360 h. This trend goes on above − 0.6 A cm^{-2} (Fig. 6d), R_p decreases when the applied current increases. In the same way as at 288 h, this trend leads at 360 h to the appearance of the negative loop for the highest current densities applied and to the change over of R_p to negative values (Fig. 6e–f). Here as well, current circulation is no longer based on the redox reactions at the electrodes but mainly on electronic conduction of YSZ electrolyte. The increase

Fig. 7 *Post-mortem* SEM cross sections of the tested cell. **a** Numerous pores and cracks observed, as well as microstructural changes at the different layers, as follows from bottom to top: Ni-YSZ electrode functional layer, YSZ electrolyte, YDC intermediary layer, LSCF electrode. **b** Delamination along the YSZ/YDC interface. **c** Delamination along both YDC/LSCF and YSZ/YDC interfaces. **d**–**f** Zoom showing numerous porosities and cracks along YSZ electrolyte, including at grain boundaries, leading to interface delamination. **g** Zoom of the internal pores formed at the YDC intermediate layer. **h** Zoom showing the microstructural changes of the Ni-YSZ functional layer near YSZ electrolyte
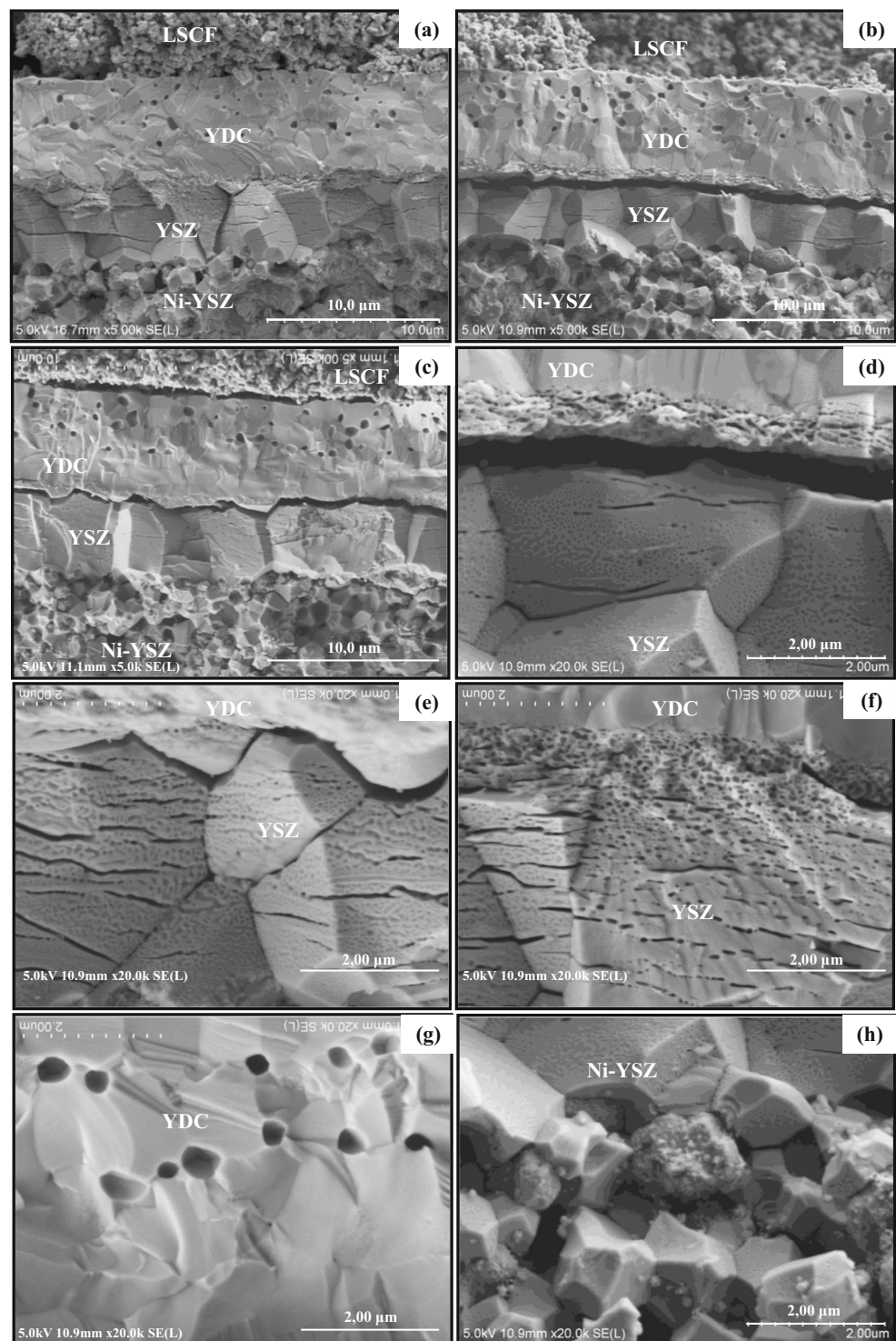

with time of R_s, as observed in Fig. 4b and for all the diagrams shown in Fig. 6, is a sign of the electrolyte degradation. The influence of the degradation becomes more dominant with time, due to the continued forced reduction of the YSZ. It should be noted that the sequence of impedance measurements at 288 and 360 h shows that at low polarization conditions, the electronic conductivity

of the YSZ electrolyte disappears, meaning that the reduction of YSZ appears to be reversible.

Post-mortem analysis

According to the SEM/EDX analysis realized on the cell after 360 h of test, several differences were found between this cell

Fig. 8 SEM images of the "craters" observed at the O_2 electrode side of the cell but outside from the LSCF surface (YDC not covered by LSCF). **a** Near LSCF. **b** Further on YDC area. **c** Zoom of the "crater." **d** Zoom showing the microstructure inside the "crater"
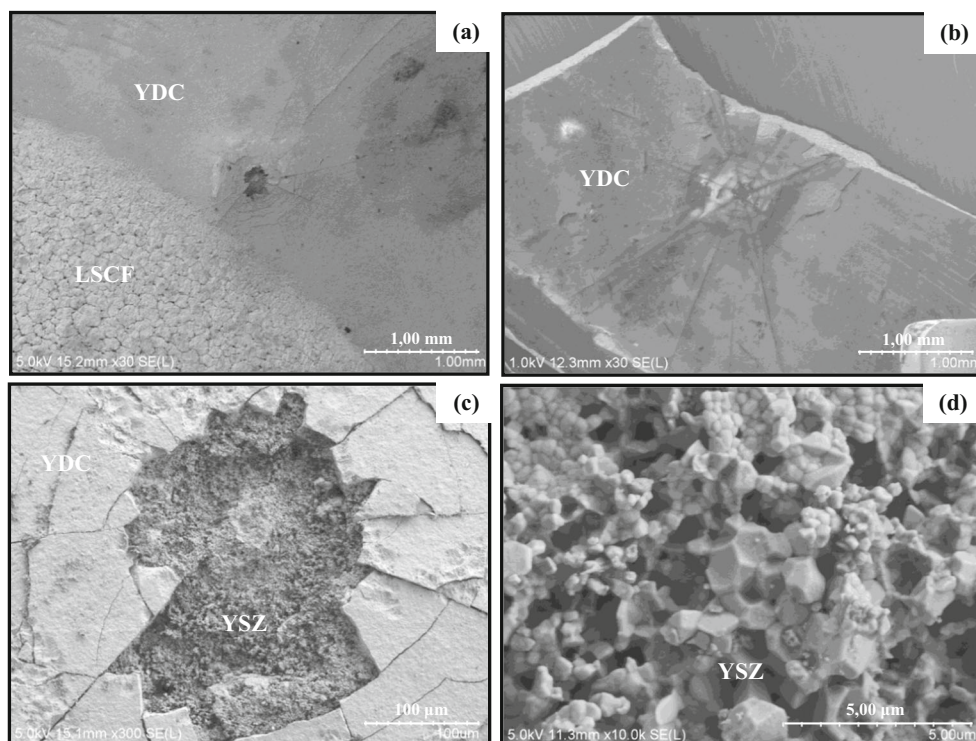
and the ones for which region VI of the *i-U* curve was not observed [4, 34].

Figure 7 shows detrimental degradation of the electrolyte characterized by the formation of numerous porosities at the grains and the grain boundaries of YSZ, often leading to the formation of cracks (Fig. 7a–f). Delamination at the YDC/ LSCF and YSZ/YDC interfaces can also be seen (Fig. 7b– c). In the case of the YSZ/YDC interface, this delamination results from formation of numerous micropores along this interface (Fig. 7d, f), including at the grain boundaries (Fig. 7e). Similar degradation was observed by Tietz et al. after 9000 h of test at $i = -1.0$ A cm^{-2} with $T \approx 780$ °C, $PH_2O/ PH_2 = 8$ on both cathode and anode sides [38], but also by Laguna-Bercero et al. during tests realized applying up to − 2.5 A cm^{-2} [24]. These two mentioned cases strengthen the

idea that, in our case, an accelerated degradation of the cell happened during our test, which lasted only 360 h, as a consequence of the electronic conduction of the YSZ electrolyte forced by applying up to − 1.7 A cm^{-2} with $PH_2O/PH_2 = 5$. Such a state of degradation was not observed during our previous studies [4, 34]. According to Laguna-Bercero et al., formation of internal pores at the grains and the grain boundaries of YSZ is explained by the reduction of YSZ electrolyte resulting from the high current applied to the cell, which induces electronic conductivity in the electrolyte. The YSZ reduction would facilitate formation of O_2 at the grain boundaries and then the grains of YSZ, leading finally to the various degradations and delaminations observed on YSZ as well as the YSZ/YDC interface [24]. Thus, these degradations explain the R_s increase observed between 288 and 360 h (Fig. 4b). The internal pores at the YDC intermediate layer (Fig. 7g) and the microstructural changes of the Ni-YSZ layer near the electrolyte (Fig. 7h) were already observed before [4, 34] but also after a durability test of 1000 h realized applying − 0.8 A cm^{-2} at 800 °C with $PH_2O/PH_2 = 9$ on the cathode side and air at the anode side [53]. However, in all these mentioned cases, degradation of YDC and Ni-YSZ were not as advanced as in the case of the present study which lasted 360 h, meaning that degradation of YDC and Ni-YSZ is partly due to the electronic conduction of YSZ.

Formation of several "craters" on the O_2 electrode side (Fig. 8a–c), but outside from the LSCF surface (YDC not covered by LSCF), were observed. The EDX analysis (not shown) reveals that the inner part of these craters is composed

Table 1 Amounts of the elements obtained by SEM/EDX analysis for the different layers of the tested cell after 360 h with, from bottom to top: Ni-YSZ electrode functional layer, YSZ electrolyte, YDC intermediary layer, LSCF electrode. All the results are presented in atomic %. It should be noted that Si is not present in this table because it was not considered in this specific study. However, Si was present in similar amounts as what obtained in the previous work recently reported [4]

	O	Cr	Fe	Co	Ni	Sr	Y	Zr	La	Ce
LSCF	44.1	24.0	24.3	6.5	0.6	6.8	0.2	0.5	15.5	0.3
YDC	25.4	0.0	3.6	2.2	10.5	1.1	3.0	5.4	2.5	44.4
YSZ	53.4	0.0	2.0	1.0	11.0	1.0	3.9	24.3	1.6	1.1
Ni-YSZ	48.6	0.1	0.2	0.1	26.6	0.0	3.3	20.7	0.2	0.1

of Ni, Y, and Zr corresponding to the Ni-YSZ electrode. Hence, these craters result from a destruction of YDC and YSZ, once again as a consequence of YSZ electronic conduction. The microstructural changes observed at some places of these craters and shown in Fig. 8d are similar to what observed in Fig. 7h.

The EDX analysis shown in Table 1 indicates a migration of La, Sr, Co, and Fe elements from LSCF anode to YDC layer and YSZ electrolyte. Furthermore, a significant shift of Ni from Ni-YSZ cathode to YSZ and YDC is observed and also to LSCF anode in a lower proportion. These element shifts, not observed previously [4, 34], are specific to this test. However, at this point, it is still unclear how these shifts can constitute another sign of the cell degradation by YSZ electronic conduction. Further work would be necessary to demonstrate that.

Conclusions

During this study, application of high current densities to a solid oxide electrolysis cell contaminated by impurities containing Si led to the appearance of a new region on the measured i-U curves, attributed to electronic conduction of YSZ electrolyte. This phenomenon is the consequence of a critical solicitation of the cell which was in a working state where H_2O transport at the Ni-YSZ electrode limited its performances. This phenomenon is characterized by a frequency shift of the whole impedance diagram toward the lowest frequencies. This shift leads finally to the disappearance of the positive loop corresponding to R_p, in favor of the appearance of a negative loop which crosses the Z' axis at the lowest frequencies to become positive. This is characteristic of a "functioning mode" where the phenomena associated with the electrochemical redox reactions are no longer involved, the current circulating mainly via electronic conduction of YSZ electrolyte. This trend was confirmed with time. Such a characterization by EIS of YSZ electrolyte electronic conduction under electrolysis mode has not been reported in literature to date, to the best of our knowledge.

Post-mortem analysis by SEM/EDX showed that this phenomenon leads to a detrimental degradation of YSZ electrolyte after only 360 h of overall testing duration. This accelerated degradation is characterized by formation of numerous porosities at YSZ grains and grain boundaries, these porosities often leading to formation of cracks as well as delamination at the YDC/YSZ interface. Internal pore formation at YSZ grains and grain boundaries is due to YSZ reduction that facilitates O_2 formation at YSZ grain boundaries, and then grains, leading to the numerous degradations and delaminations observed. In addition, YSZ electronic conduction leads to formation of several "craters" on the O_2 electrode side but outside from the LSCF surface (YDC not covered by LSCF).

Lastly, EDX analysis revealed (i) a migration of La, Sr, Co, and Fe elements from LSCF anode to YDC layer and YSZ electrolyte and (ii) a significant shift of Ni from Ni-YSZ cathode to YSZ and YDC, and also to LSCF anode in a lower proportion. However, it is still unclear how these shifts can constitute another sign of the cell degradation by YSZ electronic conduction.

This detailed electrochemical investigation based on chronopotentiometry and EIS highlights how impurity deposit can dramatically affect the solid oxide electrolysis cell operation.

References

1. Goltsov VA, Veziroglu TN (2001) Int J Hydrog Energy 26(9):909–915
2. Rosen MA, Scott DS (1998) Int J Hydrog Energy 23(8):653–659
3. Nechache A, Cassir M, Ringuedé A (2014) J Power Sources 258:164–181
4. Nechache A, Boukamp BA, Cassir M, Ringuedé A (2018) J Solid State Electrochem. First Online https://doi.org/10.1007/s10008-018-4116-7
5. Kharton VV (ed) (2009) Solid state electrochemistry I: fundamentals, materials and their applications. Wiley, Weinheim
6. Durov AV, Naidich YV, Kostyuk BD (2005) J Mater Sci 40(9-10):2173–2178
7. Warner TE, Janes R, Edwards PP (1991) J Mater Sci Lett 10(16):937–938
8. Weininger JL, Zemany PD (1954) J Chem Phys 22(8):1469–1470
9. Jacquin M, Guillou M, Millet J (1967) CR Acad Sci 264:2101
10. Etsell TH, Flengas SN (1971) J Electrochem Soc 118(12):1890–1900
11. Brook RJ, Pelzmann WL, Kroger FA (1971) J Electrochem Soc 118(2):185–192
12. Perfilev MV, Palguev SF (1967) Electrochem Molten Solid Electrolytes 4:147
13. Bauerle JE (1969) J Phys Chem Solids 30(12):2657–2670
14. Karpachev SV, Ovchinnikov YM (1969) Soy Electrochem 5:181
15. Kleitz M. (1968) Thesis, Grenoble University
16. Yanagida H, Brook RJ, Kroger FA (1970) J Electrochem Soc 117(5):593–602
17. Tedmon CS, Spacil HS, Mitoff SP (1969) J Electrochem Soc 116(9):1170–1175
18. Gokhshstein YP, Safonov AA (1970) High Temp 8:368
19. Casselton REW (1974) J Appl Electrochem 4(1):25–48
20. Fabry P., Kleitz M. (1976) in: M. Kleitz, J. Dupuy (Eds.), Electrode processes in solid state ionics, Reidel Publ. Comp., Dordrecht, pp. 331–365
21. Janek J, Korte C (1999) Solid State Ionics 116(3-4):181–195

22. Boulfrad S, Djurado E, Fouletier J (2009) Solid State Ionics 180(14-16):978–983

23. Knibbe RML, Traulsen MLA, Hauch ASD, Ebbesen SDM, Mogensen M (2010) J Electrochem Soc 157(8):B1209–B1217

24. Laguna-Bercero MA, Campana R, Larrea A, Kilner JA, Orera VM (2011) J Power Sources 196(21):8942–8947

25. Kim J, Ji H, Dasari HP, Shin D, Song H, Lee JH, Kim BK, Je HJ, Lee HW, Yoon KJ (2013) Int J Hydrog Energy 38(3):1225–1235

26. Chen M, Liu YL, Bentzen JJ, Zhang W, Sun X, Hauch A, Tao Y, Bowen JR, Hendriksen PV (2013) J Electrochem Soc 160(8):F883–F891

27. Sun X, Chen M, Hjalmarsson P, Ebbesen SD, Jensen SH, Mogensen M, Hendriksen PV (2012) ECS Trans 41:77–85

28. Barfod R, Mogensen M, Klemenso T, Hagen A, Liu YL, Hendriksen PV (2007) J Electrochem Soc 154(4):B371–B378

29. Primdahl S, Mogensen M (1998) J Electrochem Soc 145(7):2431–2438

30. Primdahl S, Mogensen M (1999) J Electrochem Soc 146(8):2827–2833

31. Jørgensen MJ, Mogensen M (2001) J Electrochem Soc 148(5):A433–A442

32. Primdahl S (1999) Risø National Laboratory. DTU, Roskilde, Denmark

33. Schefold J, Brisse A, Tietz F (2012) J Electrochem Soc 159:A137–A144

34. Nechache A, Mansuy A, Petitjean M, Mougin J, Mauvy F, Boukamp BA, Cassir M, Ringuedé A (2016) Electrochim Acta 210:596–605

35. Leonide A, Sonn V, Weber A, Ivers-Tiffée E (2008) J Electrochem Soc 155(1):B36–B41

36. Kournoutis VC, Tietz F, Bebelis S (2009) Fuel Cells 09(6):852–860

37. Ivers-Tiffée E, Weber A (2017) J Ceram Soc Japan 125(4):193–201

38. Tietz F, Sebold D, Brisse A, Schefold J (2013) J Power Sources 223:129–135

39. Schefold J, Brisse A, Poepke H (2017) Int J Hydrog Energy 42(19):13415–13426

40. Laguna-Bercero MA (2012) J Power Sources 203:4–16

41. Moçoteguy P, Brisse A (2013) Int J Hydrog Energy 38(36):15887–15902

42. Ebbesen SD, Jensen SH, Hauch A, Mogensen MB (2014) Chem Rev 114(21):10697–10734

43. Irvine JTS, Neagu D, Verbraeken MC, Chatzichristodoulou C, Graves CR, Mogensen MB (2016) Nat Energy 1:1–13

44. Wang Y, Liu T, Lei L, Chen F (2017) J Power Sources 344:119–127

45. Keane M, Fan H, Han M, Singh P (2014) Int J Hydrog Energy 39(33):18718–18726

46. Zhang L, Zhu X, Cao Z, Wang Z, Li W, Zhu L, Li P, Huang X, Lü Z (2017) Electrochim Acta 232:542–549

47. Hauch A, Brodersen K, Chen M, Mogensen MB (2016) Solid State Ionics 293:27–36

48. Lim CK, Liu Q, Zhou J, Sun Q, Chan SH (2017) J Power Sources 342:79–87

49. Lee SJ, Jung CY, Yi SC (2017) Electrochim Acta 242:86–89

50. Boulfrad S, Nechache A, Cassidy M, Traversa E, Irvine JTS (2015) ECS Trans 68(1):2011–2018

51. Schouler EJL, Kleitz M, Forest E, Fernandez E, Fabry P (1981) Solid State Ionics 5:559–562

52. Schefold J, Brisse A, Zahid M (2009) J Electrochem Soc 156(8):B897–B904

53. Mansuy A (2012) PhD Thesis, Université Bordeaux 1, Bordeaux